

Graphene layer reinforcing mesoporous molybdenum disulfide foam as high-performance anode for sodium-ion battery

Jiao Deng ^{a, c, 1}, Cheng Zeng ^{b, 1}, Chao Ma ^d, Jon Fold von Bülow ^e, Lei Zhang ^{b, **}, Dehui Deng ^{a, c, *}, Zhongqun Tian ^a, Xinhe Bao ^c

^a State Key Laboratory of Physical Chemistry of Solid Surfaces, Collaborative Innovation Center of Chemistry for Energy Materials (iChEM), College of Chemistry and Chemical Engineering, Xiamen University, Xiamen, 361005, China

^b Key Lab of Heat Transfer Enhancement and Energy Conservation of Ministry of Education, School of Chemistry and Chemical Engineering, South China University of Technology, Guangzhou 510640, China

^c State Key Laboratory of Catalysis, Collaborative Innovation Center of Chemistry for Energy Materials (iChEM), Dalian Institute of Chemical Physics, Chinese Academy of Science, Dalian, 116023, China

^d Center for High Resolution Electron Microscopy, College of Materials Science and Engineering, Hunan University, Changsha, 410082, China

^e Haldor Topsøe A/S, Haldor Topsøes Allé 1, DK-2800, Kgs. Lyngby, Denmark



ARTICLE INFO

Article history:

Received 31 March 2018

Accepted 3 April 2018

Available online 14 April 2018

ABSTRACT

Sodium-ion batteries are currently being considered as a promising concept for large-scale energy storage. This is partly due to the low cost and abundance of sodium and the possibility to use cheaper parts on cell level such as current collector and electrolyte. As an important electrode in a safe rechargeable sodium-ion battery, the electrochemical activity on the anode involves a series of complex electrochemical processes. Therefore, new strategies for material design are required to promote each pivotal step in the optimization of battery performance. Herein, we present a multiscale design of a mesoporous MoS₂ foam with a coating of graphene layers as a highly efficient anode for sodium-ion batteries. The resulting composite material delivers impressive electrochemical performance in a half-cell versus metallic sodium with a high specific capacity for sodium ions and a stable performance during cycling for more than 1000 cycles. The strategy introduced in this study opens new opportunities, not only for the development of MoS₂ composite anode materials through a multiscale design to maintain high capacity and stability, but also for the development of other sodium-ion battery anode materials.

© 2018 Elsevier Ltd. All rights reserved.

1. Introduction

Large-scale energy storage systems (ESS) have attracted great attention owing to the increasing energy crisis and environmental problems [1–3]. As an ESS concept, the sodium-ion battery (SIB) with the advantage of low cost, high natural abundance and wide global distribution of sodium resources, is a promising alternative to the lithium-ion battery (LIB) [3–8]. Although the SIB technology shares many similarities with LIB, it is in its commercial infancy and a substantial research activity has been focused on the development

and improvement of electrode materials. The fact that e.g. commercial graphite, which is being used as an anode material in LIBs, has a very low capacity for accommodating sodium ions, makes the search for new suitable host materials necessary [9–11]. Carbonaceous materials such as hard and soft carbon are currently the most promising candidates for the anode in SIBs, because they exhibit an attractive voltage profile with stable performance, while being commercially available. However, the relatively low capacity of hard carbons with long cycle life hovers around 200–250 mA h g⁻¹ even at a low current density (e.g. 100 mA g⁻¹) [12,13], prompting the exploration into other material classes with higher capacity for sodium ions. Among the recent alternative anode materials [14–21], metal sulfides have attracted considerable interest due to their two-dimensional (2D) structure, possessing a larger layer spacing supporting the intercalation and de-intercalation of sodium ions and consequently a higher capacity [22–24]. For instance, 2D MoS₂ exhibits the S–Mo–S single layers held together by van der Waals

* Corresponding author. State Key Laboratory of Catalysis, Collaborative Innovation Center of Chemistry for Energy Materials (iChEM), Dalian Institute of Chemical Physics, Chinese Academy of Science, Dalian, 116023, China.

** Corresponding author.

E-mail addresses: celeizhang@scut.edu.cn (L. Zhang), [\(D. Deng\).](mailto:dhdeng@dicp.ac.cn)

¹ These authors contributed equally to this work.

interaction with large interlayer spacing (6.2 Å). This is beneficial to the reversible intercalation/de-intercalation of sodium ions into the weakly bound stacked layers with high mobility [25–38].

Previous studies have shown that it is of great importance to rationally design and fabricate a nanostructure of MoS₂ which would otherwise exhibit unsatisfactory electrochemical performance of low capacity and poor cycling stability [39–41]. Different strategies for making nanostructures MoS₂ have been considered, e.g. tuning morphologies with 1D to 3D structures [25,31], manufacturing hollow framework [35,36], and constructing composites with carbon materials [26,30]. However, either strategy alone only leads to limited performance improvement in the MoS₂ anode materials, because a series of complex electrochemical processes are involved in the multi-components of the SIB anode. This requires a multiscale design of MoS₂ (from nanometers to micrometers) to promote each pivotal step and thereby maximize the battery performance. It includes constructing sufficient channels for the sodium ion diffusion, facile contact for the electrolyte, abundant insertion/extraction sites for sodium ions, and preservation of the intrinsic structure of MoS₂.

Herein, we present a multiscale design of a mesoporous MoS₂ foam with a coating of graphene layers as a highly efficient anode for SIBs. The design can be described as follows: (a) uniform mesopores facilitate sodium ion diffusion and increase the contact probability of electrolyte with MoS₂; (b) oriented vertical structures provides abundant edge sites for sodium ion insertion/extraction; (c) graphene layers coated onto the MoS₂ structure enhance overall electrode conductivity meanwhile limiting the detrimental deformation of MoS₂ during the discharge/charge process. The resulting composite material delivers an impressive discharge capacity of 488 mA h g⁻¹ at 100 mA g⁻¹ after 100 cycles in a half-cell versus metallic sodium. The composite is also able to deliver a reversible capacity of 200 mA h g⁻¹ at 1000 mA g⁻¹ after 1000 cycles.

2. Results and discussion

The synthesis procedure of graphene layers coating mesoporous MoS₂ foam (mPF-MoS₂@G) is illustrated in Fig. 1a. First, a direct chemical synthesis method was adopted to prepare the bare mesoporous MoS₂ foam (mPF-MoS₂). The (NH₄)₆Mo₇O₂₄ and CS₂ were used as Mo and S sources, respectively, during the chemical reaction under 400 °C templated by colloidal SiO₂ nanospheres. The mPF-MoS₂ was obtained after etching the SiO₂ template with HF (a.q.). To further coat the graphene layers onto mPF-MoS₂, dopamine was used as the carbon source for pre-coating, which was followed by annealing at 600 °C under Ar atmosphere. The final gained sample was thin graphene layers coating mesoporous MoS₂ foam (see the experimental procedures section for details).

The transmission electron microscopy (TEM) image (Fig. 1b) and scanning electron microscopy (SEM) image (Fig. S1) exhibit that the mPF-MoS₂ possesses a uniform mesoporous framework. Besides, these mesopores are interconnected throughout the entire 3D MoS₂ foam at different orientations by 3D tomography (Fig. S2), which can facilitate the diffusion of sodium ions and increase electrolyte contact to the MoS₂ surface during the discharge/charge processes. Furthermore, high resolution TEM (HRTEM) image (Fig. S3) and high resolution high-angle annular dark field-scanning transmission electron microscopy (HR-HAADF-STEM) image (Fig. 1c) distinctly display massive vertically aligned MoS₂ layers, indicating a large number of edges are exposed which will provide more sites for the sodium ion insertion/extraction. After graphene layers coating, the mPF-MoS₂@G still retains the structure of mesoporous foam according to the TEM and HAADF-STEM images (Fig. S4 and Fig. 1d). The energy-dispersive X-ray (EDX) maps show that the Mo, S and C

elements were distributed homogeneously in the porous framework (Fig. 1d), illustrating the uniform coating of graphene layers on MoS₂. In addition, through the HRTEM images (Fig. 1e and f), the contour lines of graphene layers around the mesoporous MoS₂ can be clearly observed. The interlayer distance of 0.38 nm and 0.62 nm corresponding to the (002) planes of graphene and MoS₂ on the two sides of the outline demonstrate that the graphene layers have been well coated onto the mesoporous MoS₂ foam, and the graphene layers were quite thin with only few layers (Fig. 1f). The thin graphene layers coating on the mesoporous foam can increase the overall electrode conductivity and provide a buffer space to withstand the detrimental deformation of MoS₂ during the discharge/charge processes.

The thin feature of graphene layers outside the mPF-MoS₂ can also be supported by the X-ray diffraction (XRD) patterns, showing no visible appearance of C (002) peak except for the diffraction peaks of hexagonal 2H-MoS₂ after coating graphene layers (Fig. 2a). Despite this, the thin graphene layers can be detected by the Raman spectra showing the extra G characteristic peak (1582 cm⁻¹) of graphene besides the E_{2g}¹ and A_{1g} modes of MoS₂ in mPF-MoS₂@G (Fig. 2b and Fig. S5). The D band (1370 cm⁻¹) of Raman spectra indicates that defects are included in the graphene layers, consistent with the result of TEM image (Fig. 1e). The coating process of graphene layers will not bring intrinsic structure variation in mPF-MoS₂, according to the X-ray absorption near-edge structure (XANES) spectra and the extended X-ray absorption fine structure (EXAFS) spectra showing similar Mo valence state, Mo–S and Mo–Mo coordinate bonds (Fig. 2c). In addition, through the similar specific surface area and pore volume in mPF-MoS₂ (96.4 m² g⁻¹, 0.654 cm³ g⁻¹) and mPF-MoS₂@G (73.7 m² g⁻¹, 0.513 cm³ g⁻¹) (Fig. 2d), the mesoporous framework has been well preserved after the graphene layers coating. Moreover, the carbon content in mPF-MoS₂@G was estimated to be 18.6 wt% as measured by the thermogravimetric analysis (TGA) (Fig. S6).

The electrochemical properties of the mPF-MoS₂@G as the anode material for SIBs were investigated as shown in Fig. 3. Firstly, the cyclic voltammograms (CV) of the mPF-MoS₂@G at a scan rate of 0.05 mV s⁻¹ over the voltage ranges of 0.05–3 V (vs. Na/Na⁺) were recorded for the initial five cycles (Fig. 3a). In the first cathodic scan, the peaks at 1.2 V and 0.8 V are related to the insertion of Na⁺ into MoS₂ interlayers and the formation of solid-electrolyte-interphase (SEI) film owing to the decomposition of the electrolyte [25,33]. The inconspicuous peak at 0.35 V is assigned to the conversion reaction of MoS₂ to Mo metal and Na₂S [42]. In the first anodic scan, a broad oxidation peak from 1.5 to 2.0 V was observed, which corresponded to the oxidation of the Mo metal to MoS₂ [28,43,44]. Furthermore, the reduction and oxidation peaks have been almost overlapped from the third cycle, suggesting the high reversibility and cycling stability of Na⁺ storage in the mPF-MoS₂@G. Compared with that of mPF-MoS₂@G, CV scans of mPF-MoS₂ with weak cathodic peaks suggest the labile formation of SEI film and quick decline of capacities in the following cycles (Fig. S7). Then, the galvanostatic discharge/charge voltage curves of mPF-MoS₂@G at 50 mA g⁻¹ over the voltage ranges of 0.05–3.0 V (vs. Na/Na⁺) were measured (Fig. 3b). Two plateaus in the ranges of 1.4–1.0 V and 0.4–0.05 V with a slope in the range of 0.9–0.5 V were observed for the first discharge profile, and a slope at 1.5–2.0 V appeared in the first charge profile, consistent with the CV results. The initial discharge capacity of mPF-MoS₂@G was up to 1470 mA h g⁻¹, much better than those of previously reported MoS₂ composite anodes [28,29,43,44]. Instead, the initial charge capacity was 661 mA h g⁻¹. The formation of dense SEI layer, as well as the pulverization of electrode and possible side reaction due to the large pore volume and ultrathin nanosheets of mPF-MoS₂@G may result in the low initial Coulombic efficiency [25,29,42]. From the

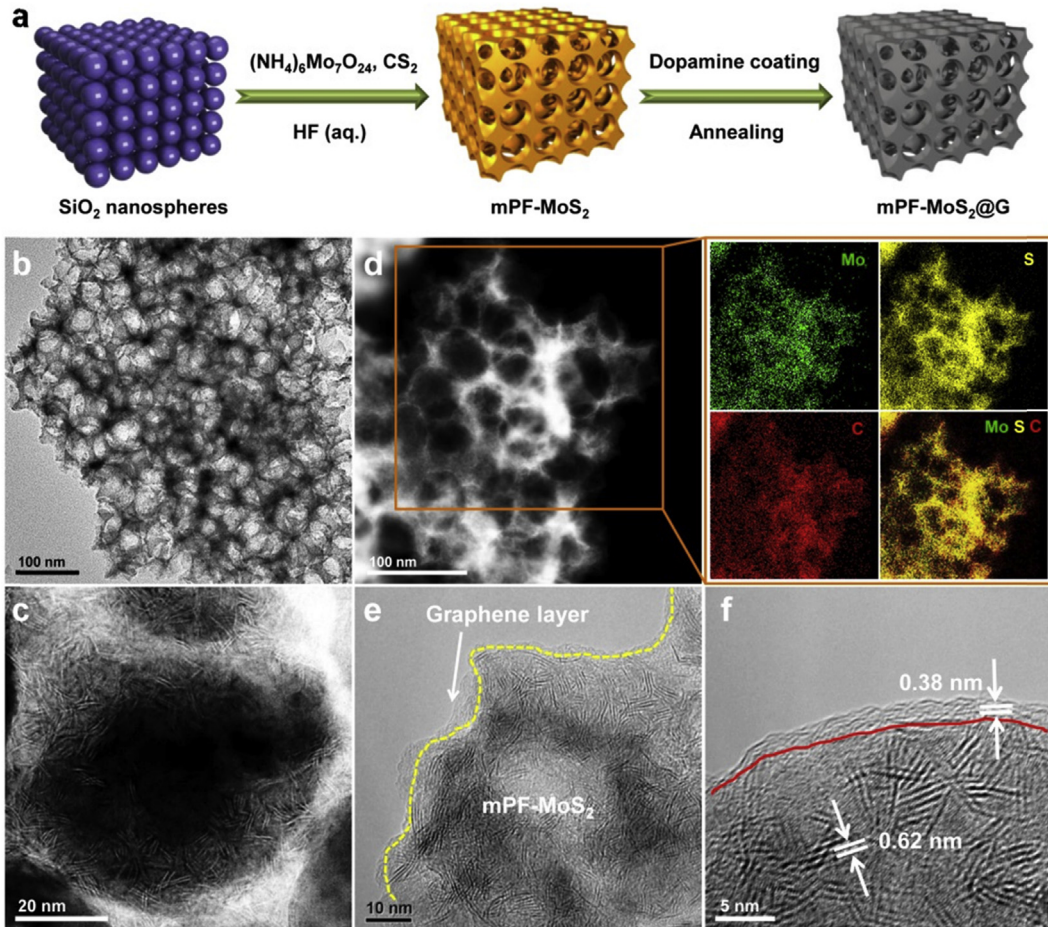


Fig. 1. Schematic illustration and morphology analysis of mPF-MoS₂ and mPF-MoS₂@G. (a) Schematic illustration of the preparation of graphene layers coating mesoporous MoS₂ foam. (b) TEM image of mPF-MoS₂. (c) High resolution HAADF-STEM of mPF-MoS₂. (d) HAADF-STEM image and corresponding EDX maps of mPF-MoS₂@G. (e) HRTEM image of mPF-MoS₂@G with inset showing a yellow contour line of graphene layers around the mesoporous MoS₂. (f) HRTEM image of mPF-MoS₂@G with inset showing a typical MoS₂ layer distance of 0.62 nm and a graphene layer distance of 0.38 nm on the two sides of the red line. (For interpretation of the references to color/colour in this figure legend, the reader is referred to the Web version of this article).

second cycle, the discharge/charge profiles are almost the same, with stable capacity retentions of 85.6%. The first cycle is an important parameter for the commercial applicability of an anode material, since the consumption of Na-ions by the anode ultimately has to be accounted for with excess capacity in the cathode of a full cell. For commercial interests, this aspect would need to be addressed in the future.

The SIB cycling performance of mPF-MoS₂@G was evaluated (the data were tested from different batches of batteries and have all been optimized). As shown in Fig. 3c, at a current density of 100 mA g⁻¹, compared with the mPF-MoS₂ without surface graphene layers showing faster capacity fading to 62 mA h g⁻¹ after 100 cycles, the mPF-MoS₂@G showed a high capacity of 488 mA h g⁻¹ (theoretical capacity of 670 mA h g⁻¹). According to the SEM image (Fig. S8a) after 100 cycles, the mesoporous framework of mPF-MoS₂@G has been well remained. Instead, the structure of mPF-MoS₂ without the protection of graphene layers has been badly destroyed (Fig. S8b), indicating the importance of graphene layers to the good cycling performance of mPF-MoS₂@G. Furthermore, the rate capabilities of the two anodes were also evaluated at various current densities ranging from 50 to 1000 mA g⁻¹ (1000 mA g⁻¹ = 1.5 C) (Fig. 3d). The average capacities of mPF-MoS₂@G were 502, 399, 353, 304 and 275 mA h g⁻¹ at current densities of 50, 100, 200, 500 and 1000 mA g⁻¹ separately, which are much higher than those of mPF-MoS₂. When the current density

returned to 50 mA g⁻¹, a stable and high discharge capacity of 450 mA h g⁻¹ for mPF-MoS₂@G can be maintained after 30 cycles, while mPF-MoS₂ showed faster capacity fading. The commercial application of an advanced SIBs needs the anode material to possess a stable cycle life. Therefore, long-term cycling test for mPF-MoS₂@G at 1000 mA g⁻¹ (1.2 mA cm⁻²) was conducted (Fig. 3e). The reversible capacities of mPF-MoS₂@G deliver 200 mA h g⁻¹ (0.24 mA h cm⁻²) after 1000 cycles with high Coulombic efficiency of 99.2%. Compared with the reported MoS₂-based anode materials, the mPF-MoS₂@G shows an advantage of long-term cycles with a stable capacity (Table S1). After 1000 cycles, although lots of the mesopores have been blocked, the basic skeleton has been kept through the SEM image (Fig. S9). The excellent discharge capacity, rate capability and cycling stability of mPF-MoS₂@G can be attributed to the multiscale design in MoS₂. Specially, the mesoporous MoS₂ foam with sufficient void space can accelerate the sodium ion diffusion through the electrode interior and increase the contact probability of electrolyte with electrode material [29,45]. Moreover, the favorable oriented structure with abundant edge sites can facilitate the sodium ion insertion/extraction [45,46]. Finally, the coated graphene layers can not only enhance the overall electrode conductivity, but also can mitigate the mechanical stress and volume expansion accompanied with the structure destruction and aggregation of MoS₂ during the discharge/charge processes [29,44,47].

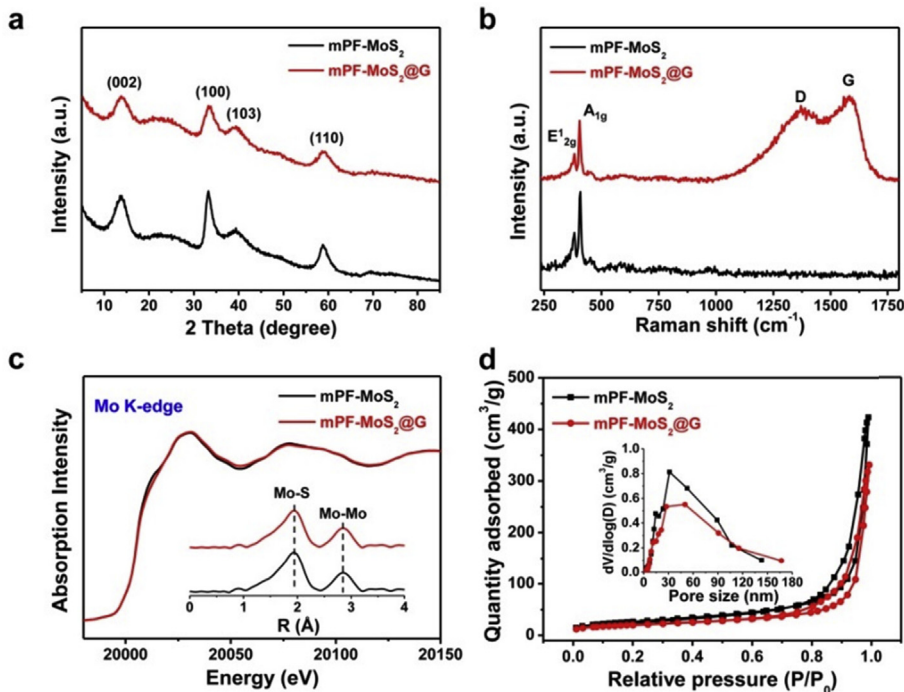


Fig. 2. Structural characterization of mPF-MoS₂ and mPF-MoS₂@G. (a) XRD patterns of mPF-MoS₂@G in comparison to mPF-MoS₂. (b) Raman spectra of mPF-MoS₂@G in comparison to mPF-MoS₂. (c) Normalized Mo K-edge XANES spectra and k²-weighted EXAFS spectra (inset) of mPF-MoS₂@G in comparison to mPF-MoS₂. (d) N₂ adsorption-desorption isotherms and pore size distribution (inset) of mPF-MoS₂@G in comparison to mPF-MoS₂.

In summary, we introduce a multiscale design of MoS₂ anode material to maintain a high and stable capacity in SIBs. The mesoporous foam with advantages of uniform mesopores and massive edge sites can facilitate the sodium ion diffusion and insertion/extraction as well as the electrolyte contact of MoS₂, which promote the MoS₂ anode to exhibit a high discharge/charge capacity and a good rate performance. The thin graphene layers coating on the mesoporous foam can provide a buffer space to withstand the detrimental deformation of MoS₂ and increase the overall electrode conductivity, which assist the mesoporous MoS₂ foam to keep a high capacity retention. Through the strategy, the final thin graphene layers coating mesoporous MoS₂ foam (mPF-MoS₂@G) delivers a high discharge capacity of 488 mA h g⁻¹ at 100 mA g⁻¹ after 100 cycles and a reversible capacity of 200 mA h g⁻¹ at 1000 mA g⁻¹ after 1000 cycles with high Coulombic efficiency of 99.2% in a half-cell versus metallic sodium. The findings in the present work pave a rational way to achieve stable high-performance of MoS₂ via a multiscale design, and the involved concept and strategy can be extended to other SIB anode materials.

3. Experimental procedures

3.1. Materials synthesis

To prepare the mPF-MoS₂ sample, 0.4 g (NH₄)₆Mo₇O₂₄·4H₂O and 1.6 g SiO₂ nanospheres (30 wt% SiO₂ in ethylene glycol, Alfa Aesar) were dispersed in 20 mL deionized water firstly. Then, after removing the solvent, the obtained powder reacted with 10 mL CS₂ in a 40 mL stainless steel autoclave at 400 °C for 4 h. The final product was gain by treating in HF (aq.) under room temperature for 5 h followed with water washing and drying processes (Caution: CS₂ and HF are hazardous liquids). To further synthesize the mPF-MoS₂@G sample, 50 mg mPF-MoS₂ and 100 mg Trizma® base were dispersed in 80 mL deionized water and maintained by

ultrasounding for 30 min. Then 32 mg dopamine hydrochloride was added followed by stirring for 5 h. After water washing and drying processes, the gain powder was treated at 600 °C under Ar atmosphere for 2 h.

3.2. Materials characterization

Scanning electron microscopy (SEM) was conducted on Hitachi S4800 and SU8220. Transmission electron microscopy (TEM), high angle annular dark field-scanning transmission electron microscopy (HAADF-STEM) and energy dispersive X-ray (EDX) mapping were carried out on a FEI Tecnai 30 microscope and a 20 microscope operated at an accelerating voltage of 300 kV and 200 kV, respectively. The high resolution HAADF-STEM and 3D tomography were carried out on the FEI Talos F200X microscope operated at 200 kV. X-ray diffraction (XRD) measurements were conducted on a Rigaku Ultima IV diffractometer with Cu K α radiation at 35 kV and 15 mA. Raman spectroscopy was performed on a Renishaw invia Raman microscope with a 532 nm excitation laser. XANES and EXAFS were measured at the BL14W1 beamline of the Shanghai Synchrotron Radiation Facility (SSRF). N₂ adsorption-desorption was measured with a Micromeritics Tristar 3020 Surface Area and Porosimetry analyzer. Thermogravimetric analysis (TGA) was performed on a TG209F1 instrument.

3.3. Electrochemical measurements

Electrochemical experiments were performed using two-electrode CR2032 coin cells. The working electrode slurry was prepared by mixing the active material, Super P, and polyvinylidene fluoride binder at a weight ratio of 6:3:1, which were then pasted onto a Cu foil current collector and dried in a vacuum oven at 60 °C for 12 h. The as-prepared electrodes possess a typical loading of the active material about 1.2 mg cm⁻². Metallic sodium foils were used

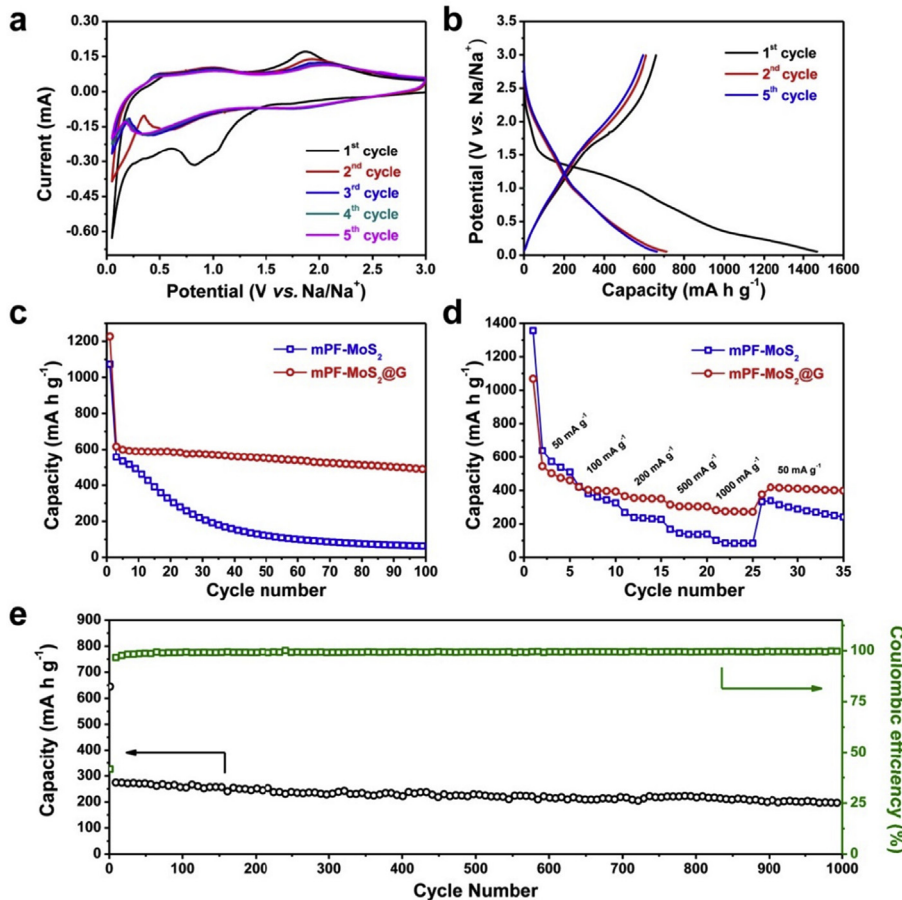


Fig. 3. Electrochemical measurements of mPF-MoS₂ and mPF-MoS₂@G. (a) CV curves of the mPF-MoS₂@G for the first five cycles at a scan rate of 0.05 mV s⁻¹. (b) Galvanostatic discharge/charge voltage curves of the mPF-MoS₂@G at a current density of 50 mA g⁻¹. (c) Cycling performances of the mPF-MoS₂@G in comparison to mPF-MoS₂ at a current density of 100 mA g⁻¹. (d) Rate performances of the mPF-MoS₂@G in comparison to mPF-MoS₂ at current densities ranging from 50 to 1000 mA g⁻¹. (e) Long-term cycling property and Coulombic efficiency of the mPF-MoS₂@G at a density of 1000 mA g⁻¹.

as counter electrodes and reference electrodes, a glass fiber membrane (Whatman/F) as a separator, the solution of 1 M NaClO₄ in a 1:1 vol mixture of ethylene carbonate/diethyl carbonate (EC/DEC) with 5 wt% fluoroethylene carbonate (FEC) as the electrolyte. A NEWARE battery testing system was applied to test galvanostatic discharge/charge cycles at different current densities in the voltage range of 0.05–3 V. The specific capacities described in this study were based on the total weight of mPF-MoS₂ or mPF-MoS₂@G. Cyclic voltammetry (CV) was measured by GAMRY instrument in a voltage range of 3–0.05 V vs. Na/Na⁺ at a scanning rate of 0.05 mV s⁻¹ at room temperature.

Author contributions

D. H. D. and L. Z. conceived the project and designed the experiments. J. D. performed the materials synthesis and materials characterization. C. Z. conducted the electrochemical measurements. C. M. performed the HR-HAADF-STEM and 3D tomography. Z. Q. T. and X. H. B. gave the valuable discussions and suggestions. J. D., C. Z., J. F. V. B., L. Z. and D. H. D. co-wrote the manuscript.

Acknowledgments

We gratefully acknowledge the financial support from the Ministry of Science and Technology of China (No. 2016YFA0204100, 2016YFA0200200 and 2016YFA0202604), the National Natural

Science Foundation of China (No. 21573220, 21621063, 21606088 and 51621001), the Key Research Program of Frontier Sciences of the Chinese Academy of Sciences (No. QYZDB-SSW-JSC020), the “Thousand Talents Program”, and the Danish company Haldor Topsøe A/S. We thank staff at the BL14W1 beamline of the Shanghai Synchrotron Radiation Facilities (SSRF) for assistance with the XANES and EXAFS measurements.

Appendix A. Supplementary data

Supplementary data related to this article can be found at <https://doi.org/10.1016/j.mtener.2018.04.001>.

References

- [1] Z.G. Yang, J.L. Zhang, M.C.W. Kintner-Meyer, X.C. Lu, D.W. Choi, J.P. Lemmon, J. Liu, Electrochemical energy storage for green grid, *Chem. Rev.* 111 (2011) 3577–3613.
- [2] B. Dunn, H. Kamath, J.M. Tarascon, Electrical energy storage for the grid: a battery of choices, *Science* 334 (2011) 928–935.
- [3] D. Larcher, J.M. Tarascon, Towards greener and more sustainable batteries for electrical energy storage, *Nat. Chem.* 7 (2015) 19–29.
- [4] S.Y. Hong, Y. Kim, Y. Park, A. Choi, N.S. Choi, K.T. Lee, Charge carriers in rechargeable batteries: Na ions vs. Li ions, *Energy Environ. Sci.* 6 (2013) 2067–2081.
- [5] S.W. Kim, D.H. Seo, X.H. Ma, G. Ceder, K. Kang, Electrode materials for rechargeable sodium-ion batteries: potential alternatives to current lithium-ion batteries, *Adv. Energy Mater.* 2 (2012) 710–721.

- [6] W.J. Liu, J.J. Jiang, H. Wang, C.X. Deng, F. Wang, G.C. Peng, Influence of graphene oxide on electrochemical performance of Si anode material for lithium-ion batteries, *J. Energy Chem.* 25 (2016) 817–824.
- [7] L. Zhang, G.Q. Zhang, H.B. Wu, L. Yu, X.W. Lou, Hierarchical tubular structures constructed by carbon-coated SnO₂ nanoplates for highly reversible lithium storage, *Adv. Mater.* 25 (2013) 2589–2593.
- [8] L. Zhang, H.B. Wu, X.W. Lou, Iron-oxide-based advanced anode materials for lithium-ion batteries, *Adv. Energy Mater.* 4 (2014) 1300958.
- [9] Y. Wen, K. He, Y.J. Zhu, F.D. Han, Y.H. Xu, I. Matsuda, Y. Ishii, J. Cumings, C.S. Wang, Expanded graphite as superior anode for sodium-ion batteries, *Nat. Commun.* 5 (2014) 4033.
- [10] D. Kundu, E. Talaie, V. Duffort, L.F. Nazar, The emerging chemistry of sodium ion batteries for electrochemical energy storage, *Angew. Chem. Int. Ed.* 54 (2015) 3431–3448.
- [11] V. Palomares, M. Casas-Cabanas, E. Castillo-Martinez, M.H. Han, T. Rojo, Update on Na-based battery materials. A growing research path, *Energy Environ. Sci.* 6 (2013) 2312–2337.
- [12] H.Y. Kang, Y.C. Liu, K.Z. Cao, Y. Zhao, L.F. Jiao, Y.J. Wang, H.T. Yuan, Update on anode materials for Na-ion batteries, *J. Mater. Chem. A* 3 (2015) 17899–17913.
- [13] Y.L. Cao, L.F. Xiao, M.L. Sushko, W. Wang, B. Schwenzer, J. Xiao, Z.M. Nie, L.V. Saraf, Z.G. Yang, J. Liu, Sodium ion insertion in hollow carbon nanowires for battery applications, *Nano Lett.* 12 (2012) 3783–3787.
- [14] V. Simone, A. Boulineau, A. de Geyer, D. Rouchon, L. Simonin, S. Martinet, Hard carbon derived from cellulose as anode for sodium ion batteries: dependence of electrochemical properties on structure, *J. Energy Chem.* 25 (2016) 761–768.
- [15] Y. Liu, F.F. Fan, J.W. Wang, Y. Liu, H.L. Chen, K.L. Jungjohann, Y.H. Xu, Y.J. Zhu, D. Bigio, T. Zhu, et al., In situ transmission electron microscopy study of electrochemical sodiation and potassiation of carbon nanofibers, *Nano Lett.* 14 (2014) 3445–3452.
- [16] Y. Kim, Y. Park, A. Choi, N.S. Choi, J. Kim, J. Lee, J.H. Ryu, S.M. Oh, K.T. Lee, An amorphous red phosphorus/carbon composite as a promising anode material for sodium ion batteries, *Adv. Mater.* 25 (2013) 3045–3049.
- [17] J. Liu, Y.R. Wen, P.A. van Aken, J. Maier, Y. Yu, Facile synthesis of highly porous Ni-Sn intermetallic microcages with excellent electrochemical performance for lithium and sodium storage, *Nano Lett.* 14 (2014) 6387–6392.
- [18] S. Yuan, X.L. Huang, D.L. Ma, H.G. Wang, F.Z. Meng, X.B. Zhang, Engraving copper foil to give large-scale binder-free porous CuO arrays for a high-performance sodium-ion battery anode, *Adv. Mater.* 26 (2014) 2273–2279.
- [19] M. Gu, A. Kushima, Y.Y. Shao, J.G. Zhang, J. Liu, N.D. Browning, J. Li, C.M. Wang, Probing the failure mechanism of SnO₂ nanowires for sodium-ion batteries, *Nano Lett.* 13 (2013) 5203–5211.
- [20] Y. Sun, L. Zhao, H.L. Pan, X. Lu, L. Gu, Y.S. Hu, H. Li, M. Armand, Y. Ikuhara, L.Q. Chen, et al., Direct atomic-scale confirmation of three-phase storage mechanism in Li₄Ti₅O₁₂ anodes for room-temperature sodium-ion batteries, *Nat. Commun.* 4 (2013) 1870.
- [21] H.L. Pan, X. Lu, X.Q. Yu, Y.S. Hu, H. Li, X.Q. Yang, L.Q. Chen, Sodium storage and transport properties in layered Na₂Ti₃O₇ for room-temperature sodium-ion batteries, *Adv. Energy Mater.* 3 (2013) 1186–1194.
- [22] T.F. Zhou, W.K. Pang, C.F. Zhang, J.P. Yang, Z.X. Chen, H.K. Liu, Z.P. Guo, Enhanced sodium-ion battery performance by structural phase transition from two-dimensional hexagonal-SnS₂ to orthorhombic-SnS, *ACS Nano* 8 (2014) 8323–8333.
- [23] S.H. Choi, Y.C. Kang, Sodium ion storage properties of WS₂-decorated three-dimensional reduced graphene oxide microspheres, *Nanoscale* 7 (2015) 3965–3970.
- [24] D.W. Su, S.X. Dou, G.X. Wang, WS₂@graphene nanocomposites as anode materials for Na-ion batteries with enhanced electrochemical performances, *Chem. Commun.* 50 (2014) 4192–4195.
- [25] S.H. Choi, Y.N. Ko, J.K. Lee, Y.C. Kang, 3D MoS₂-graphene microspheres consisting of multiple nanospheres with superior sodium ion storage properties, *Adv. Funct. Mater.* 25 (2015) 1780–1788.
- [26] Z.T. Shi, W.P. Kang, J. Xu, Y.W. Sun, M. Jiang, T.W. Ng, H.T. Xue, D.Y.W. Yu, W.J. Zhang, C.S. Lee, Hierarchical nanotubes assembled from MoS₂-carbon monolayer sandwiched superstructure nanosheets for high-performance sodium ion batteries, *Nano Energy* 22 (2016) 27–37.
- [27] X. Xu, D.M. Yu, H. Zhou, L.S. Zhang, C.H. Xiao, C.W. Guo, S.W. Guo, S.J. Ding, MoS₂ nanosheets grown on amorphous carbon nanotubes for enhanced sodium storage, *J. Mater. Chem. A* 4 (2016) 4375–4379.
- [28] Y.X. Wang, K.H. Seng, S.L. Chou, J.Z. Wang, Z.P. Guo, D. Wexler, H.K. Liu, S.X. Dou, Reversible sodium storage via conversion reaction of a MoS₂-C composite, *Chem. Commun.* 50 (2014) 10730–10733.
- [29] Y.L. Ding, P. Kopold, K. Hahn, P.A. van Aken, J. Maier, Y. Yu, A lamellar hybrid assembled from metal disulfide nanowall arrays anchored on a carbon layer: in situ hybridization and improved sodium storage, *Adv. Mater.* 28 (2016) 7774–7782.
- [30] X.Q. Xie, Z.M. Ao, D.W. Su, J.Q. Zhang, G.X. Wang, MoS₂/graphene composite anodes with enhanced performance for sodium-ion batteries: the role of the two-dimensional heterointerface, *Adv. Funct. Mater.* 25 (2015) 1393–1403.
- [31] W.H. Ryu, J.W. Jung, K. Park, S.J. Kim, I.D. Kim, Vine-like MoS₂ anode materials self-assembled from 1-D nanofibers for high capacity sodium rechargeable batteries, *Nanoscale* 6 (2014) 10975–10981.
- [32] J.J. Wang, C. Luo, T. Gao, A. Langrock, A.C. Mignerey, C.S. Wang, An advanced MoS₂/carbon anode for high-performance sodium-ion batteries, *Small* 11 (2015) 473–481.
- [33] L. David, R. Bhandavat, G. Singh, MoS₂/graphene composite paper for sodium-ion battery electrodes, *ACS Nano* 8 (2014) 1759–1770.
- [34] Z. Hu, L.X. Wang, K. Zhang, J.B. Wang, F.Y. Cheng, Z.L. Tao, J. Chen, MoS₂ nanoflowers with expanded interlayers as high-performance anodes for sodium-ion batteries, *Angew. Chem. Int. Ed.* 53 (2014) 12794–12798.
- [35] Y. Wang, Q.T. Qu, G.C. Li, T. Gao, F. Qian, J. Shao, W.J. Liu, Q. Shi, H.H. Zheng, 3D interconnected and multiwalled carbon@MoS₂@carbon hollow nanocables as outstanding anodes for Na-ion batteries, *Small* 12 (2016) 6033–6041.
- [36] F. Shen, W. Luo, J.Q. Dai, Y.G. Yao, M.W. Zhu, E. Hitz, Y.F. Tang, Y.F. Chen, V.L. Sprengle, X.L. Li, et al., Ultra-thick, low-tortuosity, and mesoporous wood carbon anode for high-performance sodium-ion batteries, *Adv. Energy Mater.* 6 (2016) 1600377.
- [37] Q.Q. Li, Z.P. Yao, J.S. Wu, S. Mitra, S.Q. Hao, T.S. Sahu, Y. Li, C. Wolverton, V.P. Dravid, Intermediate phases in sodium intercalation into MoS₂ nanosheets and their implications for sodium-ion batteries, *Nano Energy* 38 (2017) 342–349.
- [38] D.W. Su, S.X. Dou, G.X. Wang, Ultrathin MoS₂ nanosheets as anode materials for sodium-ion batteries with superior performance, *Adv. Energy Mater.* 5 (2015) 1401205.
- [39] G.S. Bang, K.W. Nam, J.Y. Kim, J. Shin, J.W. Choi, S.Y. Choi, Effective liquid-phase exfoliation and sodium ion battery application of MoS₂ nanosheets, *ACS Appl. Mater. Interfaces* 6 (2014) 7084–7089.
- [40] S. Zhang, X.B. Yu, H.L. Yu, Y.J. Chen, P. Gao, C.Y. Li, C.L. Zhu, Growth of ultrathin MoS₂ nanosheets with expanded spacing of (002) plane on carbon nanotubes for high-performance sodium-ion battery anodes, *ACS Appl. Mater. Interfaces* 6 (2014) 21880–21885.
- [41] X.F. Wang, Y.J. Li, Z.R.X. Guan, Z.X. Wang, L.Q. Chen, Micro-MoS₂ with excellent reversible sodium-ion storage, *Chem. Eur. J.* 21 (2015) 6465–6468.
- [42] Y.Y. Lu, Q. Zhao, N. Zhang, K.X. Lei, F.J. Li, J. Chen, Facile spraying synthesis and high-performance sodium storage of mesoporous MoS₂/C microspheres, *Adv. Funct. Mater.* 26 (2016) 911–918.
- [43] C.B. Zhu, X.K. Mu, P.A. van Aken, Y. Yu, J. Maier, Single-layered ultrasmall nanoplates of MoS₂ embedded in carbon nanofibers with excellent electrochemical performance for lithium and sodium storage, *Angew. Chem. Int. Ed.* 53 (2014) 2152–2156.
- [44] X.Q. Xie, T. Makaryan, M.Q. Zhao, K.L. Van Aken, Y. Gogotsi, G.X. Wang, MoS₂ nanosheets vertically aligned on carbon paper: a freestanding electrode for highly reversible sodium-ion batteries, *Adv. Energy Mater.* 6 (2016) 1502161.
- [45] J. Deng, H.B. Li, S.H. Wang, D. Ding, M.S. Chen, C. Liu, Z.Q. Tian, K.S. Novoselov, C. Ma, D.H. Deng, et al., Multiscale structural and electronic control of molybdenum disulfide foam for highly efficient hydrogen production, *Nat. Commun.* 8 (2017) 14430.
- [46] Q. Zhang, S.J. Tan, R.G. Mendes, Z.T. Sun, Y.T. Chen, X. Kong, Y.H. Xue, M.H. Rummeli, X.J. Wu, S.L. Chen, et al., Extremely weak van der waals coupling in vertical ReS₂ nanowalls for high-current-density lithium-ion batteries, *Adv. Mater.* 28 (2016) 2616–2623.
- [47] L. Zhang, X.W. Lou, Hierarchical MoS₂ shells supported on carbon spheres for highly reversible lithium storage, *Chem. Eur. J.* 20 (2014) 5219–5223.